

## PAPER

[View Article Online](#)  
[View Journal](#) | [View Issue](#)Cite this: *J. Mater. Chem. C*, 2020, **8**, 13762High-performance light trajectory tracking and image sensing devices based on a  $\gamma$ - $\text{In}_2\text{Se}_3/\text{GaAs}$  heterostructure†Jing-Wei Kang,<sup>a</sup> Chao Zhang,<sup>a</sup> Kai-Jun Cao,<sup>a</sup> Yu Lu,<sup>a</sup> Chun-Yan Wu,<sup>id</sup> <sup>\*,a</sup>  
Shi-Rong Chen,<sup>a</sup> Di Wu,<sup>id</sup> <sup>b</sup> Chao Xie<sup>\*,a</sup> and Lin-Bao Luo<sup>id</sup> <sup>\*,a</sup>

In this work, we present the assembly of a  $\gamma$ - $\text{In}_2\text{Se}_3/\text{GaAs}$  heterostructure-based photodetector linear array composed of  $1 \times 10$  device units. The layered  $\gamma$ - $\text{In}_2\text{Se}_3$  films with a well-defined pattern are deposited directly onto a planar GaAs substrate via radio-frequency (RF) magnetron sputtering deposition assisted by a pre-photolithography process. The as-fabricated heterojunction exhibits an apparent photovoltaic effect, which endows the device with a function to operate as a self-driven photodetector. The critical photoresponse performance parameters in terms of the  $I_{\text{light}}/I_{\text{dark}}$  ratio, responsivity ( $R$ ), specific detectivity ( $D^*$ ) and response speed can reach  $1.29 \times 10^4$ ,  $0.25 \text{ A W}^{-1}$ ,  $7.34 \times 10^{12}$  Jones and  $23.6/146.7 \text{ } \mu\text{s}$  (rise/fall times), respectively, upon 660 nm light irradiation at 0 V. What is more, further device evaluation reveals that the photodetector array shows good uniformity with a minor unit-to-unit variation. The above merits endow the photodetector array with the ability to monitor a moving optical signal and to record an "E" image produced by visible illumination. It is believed that the present photodetector array is very promising for some optoelectronic purposes such as real-time light trajectory tracking and visible light image sensing applications.

Received 14th August 2020,  
Accepted 6th September 2020

DOI: 10.1039/d0tc03872e

[rsc.li/materials-c](http://rsc.li/materials-c)

## Introduction

As an important kind of optoelectronic device that can convert optical signals into electricity, photodetectors have demonstrated tremendous potential in both military and civil areas, such as target detection, optical communication, safety monitoring, industrial control systems and medical diagnostics.<sup>1–4</sup> Currently, commercial photodetectors operating in the ultraviolet (250–400 nm), visible (400–800 nm) and near-infrared (900–1700 nm) spectral regions have been dominated by bulk crystalline GaN, Si and InGaAs or Si/Ge heterojunctions, respectively.<sup>5,6</sup> In spite of their mature fabrication technologies and good device performance, there are some unavoidable drawbacks such as fragileness of the materials, high material usage, sophisticated manufacturing processes and critical operating requirements, which greatly hinder further development of these devices and also their potential applications in novel devices, such as flexible and stretchable devices.

Recently, numerous efforts have been made in identifying novel functional materials such as two-dimensional (2D) layered semiconductors for high-performance photodetector applications.<sup>6</sup> Group-VIB transition-metal dichalcogenides (TMDCs) (e.g.,  $\text{MoS}_2$ ,  $\text{MoSe}_2$ , and  $\text{WS}_2$ ),<sup>7,8</sup> newly discovered group-10 TMDCs (e.g.,  $\text{PdSe}_2$ ,  $\text{PtS}_2$ , and  $\text{PtSe}_2$ ),<sup>9–11</sup> group-IIIa metal chalcogenides (e.g. GaS, GaSe, InSe, and  $\text{In}_2\text{Se}_3$ ),<sup>12–14</sup> and IVA–VIA compounds (e.g.  $\text{SnSe}_2$ <sup>15</sup> and  $\text{SnSe}$ <sup>16</sup>) have emerged as prominent candidates for ultrasensitive photodetector application, due to their unique atomic structure and excellent characteristics such as strong light–material interaction, layer-dependent electronic and optoelectronic properties, improved light absorption efficiency and wonderful mechanical flexibility.<sup>17,18</sup> As an interesting group-IIIa metal chalcogenide, indium selenide ( $\text{In}_2\text{Se}_3$ ) is regarded as a promising building block for applications in high-performance photodetection and other optoelectronic devices due to its appealing material properties.<sup>19–21</sup> These features include a direct bandgap allowing a high absorption coefficient and therefore the efficient production of electron–hole pairs upon photoexcitation, with a broadband optical absorption ranging from UV to NIR enabling a wide spectral photoresponse.<sup>22,23</sup> For instance, by mechanical exfoliation from  $\text{In}_2\text{Se}_3$  bulk crystals, Yu *et al.* presented a UV-visible-NIR photodetector made of  $\sim 10 \text{ nm } \alpha\text{-In}_2\text{Se}_3$  nanosheets, which has a high responsivity of  $395 \text{ A W}^{-1}$  and a fast response of 18 ms at 300 nm.<sup>24</sup> Benefiting

<sup>a</sup> School of Electronic Science and Applied Physics, Hefei University of Technology, Hefei, Anhui 230009, P. R. China. E-mail: cywu@hfut.edu.cn, chao.xie@hfut.edu.cn, luob@hfut.edu.cn<sup>b</sup> School of Physics and Microelectronics, Zhengzhou University, Zhengzhou, Henan 450052, P. R. China. E-mail: wudi1205@zzu.edu.cn

† Electronic supplementary information (ESI) available. See DOI: 10.1039/d0tc03872e

from the oxygen absorption and oxygen-associated selenium defects, a UV-short-wavelength infrared (325–1800 nm) broadband photodetector based on exfoliated  $\alpha$ - $\text{In}_2\text{Se}_3$  layers with a photoresponse beyond the intrinsic bandgap of the material has also been demonstrated recently.<sup>25</sup> Moreover, because of the pronounced photogating effect due to the presence of long-lived trap states (e.g., the intrinsic defects or the native surface oxides), Island and his co-workers reported a multilayered  $\text{In}_2\text{Se}_3$  photodetector with an ultrahigh responsivity ( $R$ ) approaching  $10^5 \text{ A W}^{-1}$  and a large specific detectivity ( $D^*$ ) of  $\sim 3.3 \times 10^{13}$  Jones.<sup>26</sup> In addition to these photoconductors/phototransistors, photodiodes composed of  $\text{In}_2\text{Se}_3$ -based heterostructures have also been explored to optimize the current on/off ratio and improve the response speed. Recently, Fan and his colleagues presented a self-driven heterojunction photodiode consisting of  $n$ -Si and  $\gamma$ - $\text{In}_2\text{Se}_3$  nanoflower films, which has a broadband photoreponse over the UV to NIR (300–1100 nm) spectrum with a good responsivity and specific detectivity.<sup>27</sup> Meanwhile, by using the pulsed laser deposition technique, Yang *et al.* reported on the scalable fabrication of  $\beta$ - $\text{In}_2\text{Se}_3$ /Si heterojunction arrays.<sup>28</sup> These devices are sensitive in a wavelength range from 370 nm to 808 nm with an  $I_{\text{on}}/I_{\text{off}}$  ratio of  $\sim 600$  and a splendid specific detectivity of  $4.9 \times 10^{12}$  Jones. Very recently, our group demonstrated the construction of a heterojunction photodetector by direct deposition of layered  $\gamma$ - $\text{In}_2\text{Se}_3$  films onto  $n$ -Si substrates through the magnetron sputtering process.<sup>29</sup> Compared to the chemical vapor deposition technique<sup>30</sup> and the pulsed laser deposition technique,<sup>31</sup> the magnetron sputtering process avoided a high growth temperature and a high-energy laser, providing an effective and low-cost method for the large-area deposition of high quality  $\gamma$ - $\text{In}_2\text{Se}_3$  films. Owing to the existence of defect energy levels within the forbidden band, this kind of heterojunction exhibits a broadband photoresponse over a wide range of spectra (200–2000 nm) with the responsivity ( $R$ ) and the specific detectivity ( $D^*$ ) reaching  $0.57 \text{ A W}^{-1}$  and  $2.6 \times 10^{12}$  Jones, respectively.

However, the functionalities of the integrated devices for multifunctional optoelectronic applications have not been demonstrated. From the perspective of device integration, intra-device isolation and crosstalk depressing between adjacent devices are necessary, which requires precise patterning of the photoactive semiconductor. To date, patterned growth of 2D  $\text{In}_2\text{Se}_3$  layers has only been realized on mica substrates by using a combined micro-intaglio printing and van der Waals epitaxial method.<sup>32</sup> The as-grown  $\text{In}_2\text{Se}_3$  has a good sensitivity to 633 nm light illumination with a responsivity of  $\sim 1650 \text{ A W}^{-1}$ . Nevertheless, the strict epitaxial growth on the mica substrates brings about difficulties in the development of electronic/optoelectronic devices with complex architectures such as heterostructures. In addition, the material growth process is also very sophisticated. Herein, we report on the fabrication of a  $\gamma$ - $\text{In}_2\text{Se}_3$ /GaAs heterostructure-based photodetector linear array comprising  $1 \times 10$  device units. Taking advantage of the photovoltaic effect, this kind of heterojunction can work as a high-performance self-driven photodetector with the  $I_{\text{light}}/I_{\text{dark}}$

ratio, responsivity, specific detectivity and response speed reaching  $1.29 \times 10^4$ ,  $0.25 \text{ A W}^{-1}$ ,  $7.34 \times 10^{12}$  Jones and 23.6/146.7  $\mu\text{s}$  (rise/fall times), respectively, under 660 nm light illumination. In addition, the photodetector array also exhibits an excellent performance uniformity, indicating its capability of monitoring a moving light signal and recording an image pattern produced by visible light irradiation. This work will be helpful for the development of integrated 2D material/semiconductor heterostructure-based optoelectronic devices for multifunctional applications.

## Experimental

### Device fabrication

A pre-cleaned  $n$ -type (100) GaAs with a resistivity of  $0.8\text{--}9 \times 10^{-3} \Omega \text{ cm}$  was used as a substrate. A 40 nm thick  $\text{Al}_2\text{O}_3$  film serving as an insulating layer was deposited atop the GaAs substrate through atomic layer deposition (ALD, LabNanoTM 9100, Ensure Nnanotech) using trimethylaluminum ( $\text{Al}(\text{CH}_3)_3$ , TMA) as a metal precursor and  $\text{H}_2\text{O}$  as an oxidant. Photolithography was used to define a  $1 \times 10$  window array with a window size of  $600 \mu\text{m} \times 600 \mu\text{m}$  on the substrate. The substrate was then etched using a buffered oxide etchant ( $\text{HCl}:\text{H}_2\text{O} = 1:1$ ) solution for 30 min to remove the unprotected  $\text{Al}_2\text{O}_3$  film. Afterwards, another photolithography process was employed to define the  $1 \times 10$  window array with a larger window size for the deposition of the  $\gamma$ - $\text{In}_2\text{Se}_3$  film onto the exposed GaAs substrate, which was accomplished *via* radio-frequency magnetron sputtering based on our previous study.<sup>29</sup> To avoid degeneration of the photoresistor, substrate heating was not employed during the magnetron sputtering process. After lift-off, the as-deposited  $\text{In}_2\text{Se}_3$  film was annealed at  $300^\circ\text{C}$  in a nitrogen atmosphere for 30 min to improve its crystallinity. Finally, Au front and bottom electrodes to form ohmic contacts with the  $\gamma$ - $\text{In}_2\text{Se}_3$  film and GaAs, respectively, were defined through additional photolithography and electron-beam deposition processes.

### Device measurement and characterization

The morphology and composition of the as-prepared  $\gamma$ - $\text{In}_2\text{Se}_3$  films were analyzed by atomic force microscopy (AFM, Dimension Icon), X-ray diffractometry (X'Pert PRO MPD) with Cu  $K\alpha$  radiation, energy-dispersive X-ray spectroscopy (EDS, Oxford INCA, attached to TEM) and X-ray photoelectron (XPS) spectroscopy (Thermo ESCALAB250) with an Al  $K\alpha$  monochromatic source. Optoelectronic performance was characterized using a Keithley 2400 semiconductor characterization system equipped with a broadband monochromator (SP 2150, Princeton Co.) under ambient conditions at room temperature. Laser diodes with different wavelengths (660 nm, Thorlabs M660L3; 1300 nm, Thorlabs M1300L3 and 1550 nm, Thorlabs M1550L3) were used as illumination sources, whose power intensities were carefully calibrated before the measurement using a power meter (Thorlabs GmbH, PM 100D). Pulsed light with varied frequencies was used for the transient photoresponse study, which was produced by driving the laser diode employing a signal generator

(Tektronix, TDS2022B). An oscilloscope (Tektronix, TDS2012B) was then used to record the electrical signal.

## Results and discussion

A  $\gamma$ - $\text{In}_2\text{Se}_3$ /GaAs heterojunction photodetector array was fabricated by direct deposition of layered  $\gamma$ - $\text{In}_2\text{Se}_3$  films with a designed pattern onto a GaAs substrate *via* radio-frequency magnetron sputtering assisted by a photolithography process, as schematically shown in Fig. 1. The detailed fabrication process is demonstrated in the “Experimental” section. Fig. 2a and b illustrates the film, from which we can find that the film has a thickness of about 45 nm with a root mean square (RMS) roughness of about 1.24 nm. The two remarkable diffraction peaks at  $27.4^\circ$  and  $44.5^\circ$  in the X-ray diffraction (XRD) pattern corresponded to the crystal planes (006) and (300) of the hexagonal defect wurtzite structure of  $\gamma$ - $\text{In}_2\text{Se}_3$  (JCPDS no. 40-1407), respectively (Fig. 2c). Furthermore, the atomic ratio of the elements In and Se in the energy-dispersive X-ray spectrum (EDS) was determined to be 2 : 3.13 (as shown in Fig. 2d). According to our previous report,<sup>29</sup> the selenium-rich composition was attributed to the substitution of the In atom with the Se atom, which gave rise to an approximately half occupied gap state located at 0.23 eV above the valence band maximum (VBM). The half occupancy quality facilitated the electrons to jump from the VB to the gap state, producing a p-type semiconducting character of the obtained  $\gamma$ - $\text{In}_2\text{Se}_3$ . Fig. 2e and f shows the high-resolution XPS spectra of the In 3d and Se 3d core levels. The In 3d spectrum presents a doublet of In 3d<sub>5/2</sub> at 444.7 eV and of In 3d<sub>3/2</sub> at 452.3 eV, while the Se 3d spectrum can be fitted into the peaks of Se 3d<sub>5/2</sub> at 53.8 eV and Se 3d<sub>3/2</sub> at 54.6 eV, which are well consistent with the binding energies of the previously reported  $\text{In}_2\text{Se}_3$  film.<sup>33,34</sup> The absence of the binding state of the Se–O bonds at about 59 eV in the XPS spectrum further confirms the high purity of the obtained  $\gamma$ - $\text{In}_2\text{Se}_3$  film.<sup>35</sup>

The electrical properties of the typical  $\gamma$ - $\text{In}_2\text{Se}_3$ /GaAs heterojunction were characterized in the dark and under 660 nm illumination at room temperature, respectively. Fig. 3a shows the current–voltage (*I*–*V*) curves of the heterojunction in the dark. Apparently, the heterojunction exhibited a typical current rectifying behavior with a high rectification ratio of  $5.5 \times 10^4$  at  $\pm 1$  V. Considering the good ohmic contact at both the

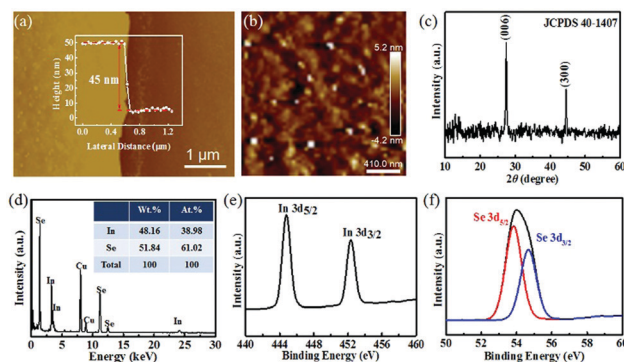


Fig. 2 (a and b) AFM image of the  $\gamma$ - $\text{In}_2\text{Se}_3$  nanofilm on the  $\text{SiO}_2/\text{Si}$  substrate. The inset in (a) shows the height profile of the nanofilm. (c) XRD pattern and (d) EDS spectrum of the  $\gamma$ - $\text{In}_2\text{Se}_3$  nanofilm. The inset in (d) shows the weight and atomic ratios of the elements In and Se. The high-resolution XPS spectra of the (e) In 3d and (f) Se 3d core levels.

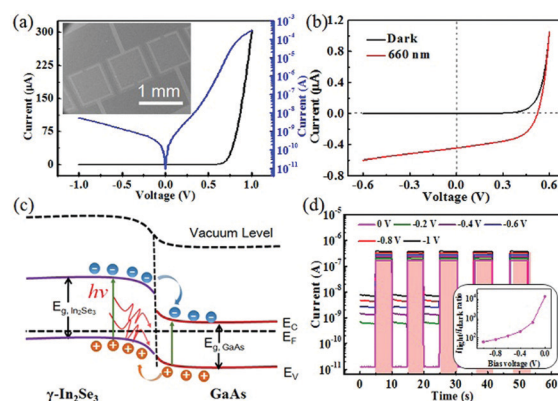


Fig. 3 (a) Typical *I*–*V* curves of the  $\gamma$ - $\text{In}_2\text{Se}_3$ /GaAs heterojunction measured in the dark (linear and semi-logarithmic scales). The inset shows a typical SEM image of the  $\gamma$ - $\text{In}_2\text{Se}_3$ /GaAs heterojunction device. (b) Typical *I*–*V* curves of the  $\gamma$ - $\text{In}_2\text{Se}_3$ /GaAs heterojunction in the dark and under 660 nm illumination with a light intensity of  $2.504 \text{ mW cm}^{-2}$ . (c) Energy band diagram of the  $\gamma$ - $\text{In}_2\text{Se}_3$ /GaAs heterojunction under light illumination at zero bias. (d) Time-dependent photoresponse of the device under 660 nm light illumination ( $0.833 \text{ mW cm}^{-2}$ ) at different bias voltages. The inset shows the  $I_{\text{light}}/I_{\text{dark}}$  ratio at different bias voltages.

Au/ $\gamma$ - $\text{In}_2\text{Se}_3$  and Au/GaAs interfaces (as shown in Fig. S1, ESI†), the above good rectifying behavior should be exclusively ascribed to the heterojunction formed at the  $\gamma$ - $\text{In}_2\text{Se}_3$ /GaAs interface.

Interestingly, when illuminated by light at 660 nm with an intensity of  $2.504 \text{ mW cm}^{-2}$ , the  $\gamma$ - $\text{In}_2\text{Se}_3$ /GaAs heterojunction displayed a remarkable photovoltaic characteristic with an open-circuit voltage ( $V_{\text{OC}}$ ) of 0.52 V and a short-circuit current ( $I_{\text{SC}}$ ) of 0.49  $\mu\text{A}$  (Fig. 3b). Such a photovoltaic behavior enables the heterojunction to operate as a self-driven photodetector, which can work without an external electrical power supply. The photoresponse characteristics of the  $\gamma$ - $\text{In}_2\text{Se}_3$ /n-GaAs heterojunction photodetector can be understood by analyzing the energy band diagram shown in Fig. 3c. When the p-type  $\gamma$ - $\text{In}_2\text{Se}_3$  film is in contact with the n-type GaAs, electrons will

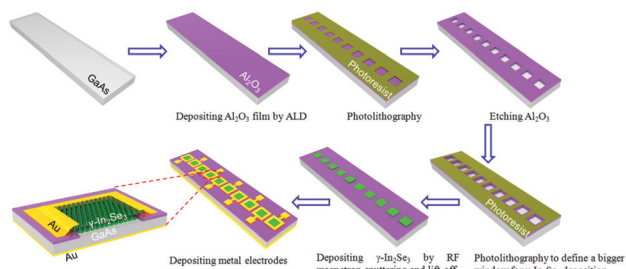


Fig. 1 Schematic diagrams of the fabrication process for the  $\gamma$ - $\text{In}_2\text{Se}_3$ /GaAs heterojunction photodetector linear array.



move from GaAs to  $\gamma$ -In<sub>2</sub>Se<sub>3</sub> until their Fermi levels are aligned at the same energy level. Accordingly, the energy levels near the surfaces of  $\gamma$ -In<sub>2</sub>Se<sub>3</sub> and GaAs will bend downward and upward, respectively, producing a built-in electric field (a depletion region) with the direction from GaAs to  $\gamma$ -In<sub>2</sub>Se<sub>3</sub> at the heterojunction interface. When the heterojunction was illuminated with incident light with the photon energy higher than the bandgaps, the photogenerated electron-hole pairs within or near the depletion region were rapidly separated toward the opposite directions by the built-in electric field. The electrons were swept into GaAs and the holes were swept into the  $\gamma$ -In<sub>2</sub>Se<sub>3</sub> layer, which were subsequently extracted by the corresponding electrodes and gave rise to the generation of photocurrent at zero bias.

Furthermore, the time-dependent photoresponse of the heterojunction at various reverse bias voltages was studied, as shown in Fig. 3d and Fig. S2 (ESI†). It was found that, for all working biases, the heterojunction could be reversibly turned between low- and high-conductance states with good repeatability, leading to a high sensitivity to the periodically switched light illumination. In addition, both the photocurrent and dark current increased monotonically with the increase in the reverse bias voltage: the former increased from 0.167  $\mu$ A to 0.372  $\mu$ A and the latter increased from 12.8 pA to 7.78 nA when the voltage changed from 0 V to −1 V. Such evolution is reasonable because a larger electric field at a negative bias voltage will restrain the carrier recombination activity by facilitating the separation of the photo-generated electron-hole pairs, and promote the carrier collection efficiency by speeding up the charge carriers.<sup>36</sup> Meanwhile, the space charge region at the heterojunction interface can be extended under reverse bias conditions, which allows more photo-generated electrons and holes to participate in the formation of photocurrent. However, because of the markedly increased dark current at reverse bias, the  $I_{\text{light}}/I_{\text{dark}}$  ratio decreased dramatically by more than two orders of magnitude, and the highest value of  $1.29 \times 10^4$  was achieved at 0 V bias.

The photoresponse of the  $\gamma$ -In<sub>2</sub>Se<sub>3</sub>/GaAs heterojunction photodetector depends strongly on the incident light intensity. Fig. 4a shows the  $I$ - $V$  curves of the heterojunction upon 660 nm illumination with different light intensities. Remarkably, both the photovoltage and photocurrent increased monotonically with the increase in the light intensity, which could be ascribed to the increased concentration of the photogenerated carriers at an evaluated light intensity. However, careful analysis revealed that the two parameters exhibited completely different evolution. The photovoltage showed a rapid increment from 0.16 to 0.48 V when the light intensity increased from 3.06  $\mu$ W cm<sup>−2</sup> to 0.833 mW cm<sup>−2</sup>, and a further increase in the light intensity led to saturation of the photovoltage (as shown in Fig. 4b). On the contrary, the photocurrent at zero bias displayed almost a linear dependence on the light intensity (Fig. 4c), and such a dependence could be well fitted by the power law:  $I_{\text{ph}} \propto P^\theta$ , where  $\theta$  is an empirical exponent, determined by the linear relationship of the light intensity and the photocurrent, reflecting the recombination ratio of

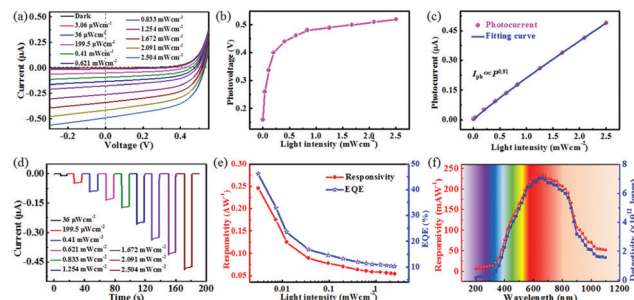


Fig. 4 (a)  $I$ - $V$  curves of the  $\gamma$ -In<sub>2</sub>Se<sub>3</sub>/GaAs heterojunction photodetector upon 660 nm light illumination with different light intensities. (b) Photovoltage and (c) photocurrent under zero bias as a function of incident light intensity. (d) Time-dependent photoresponse of the device under zero bias upon 660 nm light illumination with various light intensities. (e) Responsivity ( $R$ ) and external quantum efficiency (EQE) of the device as a function of incident light intensity. (f) Wavelength-dependent responsivity ( $R$ ) and specific detectivity ( $D^*$ ) over a wavelength range of 200–1120 nm.

the photogenerated carriers.<sup>10</sup> The fitting in the light intensity range of 3.06  $\mu$ W cm<sup>−2</sup> to 2.504 mW cm<sup>−2</sup> gave a nearly ideal  $\theta$  value of 0.91, suggesting a low recombination loss in the present heterojunction photodetector and also verifying the excellent heterojunction interface.<sup>37,38</sup> Moreover, the time-dependent photoresponse under varied light intensities was explored as well, as plotted in Fig. 4d. Apparently, the heterojunction photodetector exhibits good photo-switching properties with excellent reproducibility under all light conditions. What is more, both the rise and fall edges were found to be very steep, which indicates that the photoexcited electrons and holes could be rapidly separated and collected in the heterojunction, and also implies a fast response speed of the heterojunction photodetector. Apart from this, the heterojunction photodetector also exhibits good stability even after being stored under ambient conditions for 7 months (shown in Fig. S3, ESI†).

In order to quantitatively evaluate the photosensitivity of the  $\gamma$ -In<sub>2</sub>Se<sub>3</sub>/GaAs heterojunction photodetector, important figure-of-merit parameters, *i.e.*, responsivity ( $R$ ) and external quantum efficiency (EQE), were calculated through the following equations:<sup>39</sup>

$$R = \frac{I_{\text{ph}}}{P_{\text{in}} S} \quad (1)$$

$$\text{EQE} = \frac{hcR}{e\lambda} \quad (2)$$

where  $I_{\text{ph}}$  represents the net photocurrent ( $I_{\text{ph}}$  is obtained by subtracting the current measured in the dark from the current measured under 660 nm light illumination ( $I_{\text{light}} - I_{\text{dark}}$ );  $P_{\text{in}}$  is the incident light power;  $S$  is the effective device area (about  $3.6 \times 10^{-3}$  cm<sup>2</sup> for this device); and  $h$ ,  $c$ ,  $e$  and  $\lambda$  represent the Planck's constant ( $6.626 \times 10^{-34}$  J s), the speed of light ( $3.0 \times 10^8$  m s<sup>−1</sup>), the elementary electrical charge ( $1.6 \times 10^{-19}$  C), and the incident light wavelength, respectively. According to the above equations and parameters, the values of  $R$  and EQE reached 0.25 A W<sup>−1</sup> and 47.5%, respectively, at a low light intensity of 3.06  $\mu$ W cm<sup>−2</sup> at zero bias. Note that such an  $R$  value

**Table 1** Comparison of the key parameters between our work and other previously reported heterojunction photodetectors with similar structures

Device structure	Measurement conditions	$R$ ( $\text{A W}^{-1}$ )	$D^*$ (Jones)	$I_{\text{light}}/I_{\text{dark}}$	$\tau_r/\tau_f$	Ref.
$\gamma\text{-In}_2\text{Se}_3/\text{GaAs}$	$V = 0$ V, $\lambda = 660$ nm	0.25	$7.34 \times 10^{12}$	$1.29 \times 10^4$	23.6/146.7 $\mu\text{s}$	Our work
$\gamma\text{-In}_2\text{Se}_3/\text{Si}$	$V = 0$ V, $\lambda = 808$ nm	0.57	$2.6 \times 10^{12}$	$1.6 \times 10^4$	35/115 $\mu\text{s}$	29
$\text{PtSe}_2/\text{GaAs}$	$V = 0$ V, $\lambda = 808$ nm	0.262	$\sim 10^{12}$	$\sim 10^4$	5.5/6.5 $\mu\text{s}$	10
Graphene/GaAs	$V = 0$ V, $\lambda = 850$ nm	$1.73 \times 10^{-3}$	$\sim 10^{11}$	$\sim 10^4$	72/122 $\mu\text{s}$	40
$\text{MoS}_2/\text{GaAs}$	$V = 0$ V, $\lambda = 635$ nm	0.419	$1.9 \times 10^{14}$	—	17/31 $\mu\text{s}$	41
$\beta\text{-In}_2\text{Se}_3/\text{Si}$	$V = -4$ V, $\lambda = 532$ nm	5.9	$4.9 \times 10^{12}$	$\sim 6 \times 10^2$	< 8.3 ms	28

is far superior to that of graphene/GaAs heterojunction photodetectors ( $1.73 \text{ mA W}^{-1}$ ),<sup>40</sup> and comparable to that of other 2D layered semiconductor/GaAs heterojunction photodetectors, such as  $\text{PtSe}_2/\text{GaAs}$ <sup>10</sup> ( $0.262 \text{ A W}^{-1}$ ) and  $\text{MoS}_2/\text{GaAs}$ <sup>41</sup> ( $0.419 \text{ A W}^{-1}$ ) heterojunctions (see Table 1). Compared to the higher  $R$  value of  $\gamma\text{-In}_2\text{Se}_3/\text{Si}$ <sup>29</sup> ( $0.57 \text{ A W}^{-1}$ ), we believe that the usage of transparent top electrodes such as graphene will greatly shorten the transmission route of the separated photo-generated carriers, leading to a more effective collection. In addition, both values decreased with the increase in the light intensity (as plotted in Fig. 4e), which was likely due to the increased recombination ratio of the photogenerated charge carriers at a higher illumination intensity.<sup>42</sup>

Another important metric, the specific detectivity ( $D^*$ ) is also estimated to evaluate the ability of detecting weak optical signals from noise, according to the following equation:<sup>43</sup>

$$D^* = \frac{RS^{1/2}}{(2eI_{\text{dark}})^{1/2}} \quad (3)$$

Accordingly, the highest value of  $D^*$  was calculated to be  $7.34 \times 10^{12}$  Jones, which was higher than those of the other  $\text{In}_2\text{Se}_3$ -based heterojunction photodetectors as mentioned in previous reports (see Table 1).<sup>28,29</sup> Fig. 4f shows the values of  $R$  and  $D^*$  as a function of incident light wavelength in the range of 200–1120 nm at a fixed light intensity ( $\sim 5 \mu\text{W cm}^{-2}$ ). Obviously, the device presented a broadband photoresponse in the visible-NIR region with the peak response located at around 650 nm, which was consistent with the intrinsic optical absorption features of the  $\gamma\text{-In}_2\text{Se}_3$  film and the GaAs substrate. What is more, the device also exhibited a stable and repeatable response to the incident light with wavelengths of 1300 nm and 1550 nm (as shown in Fig. S4, ESI†). According to our previous work,<sup>29</sup> the spectral photoresponse beyond the absorption limit of both  $\gamma\text{-In}_2\text{Se}_3$  and GaAs can be ascribed to the red shift of the absorption region and the increased absorption coefficient of  $\gamma\text{-In}_2\text{Se}_3$  from visible to NIR regions after substituting In with Se atoms.

The response speed, reflecting the ability of the device to track rapidly switched optical signals, is another key parameter of a photodetector. Fig. 5a illustrates a setup for measuring the response speed in this experiment. The  $\gamma\text{-In}_2\text{Se}_3/\text{GaAs}$  heterojunction photodetector was illuminated using a 660 nm pulsed laser signal with varied frequencies driven by a signal generator and the variation of photovoltage *versus* time was recorded using an oscilloscope. The photoresponse curves of the photodetector to the pulsed light with a frequency of 1 kHz, 5 kHz and 10 kHz,

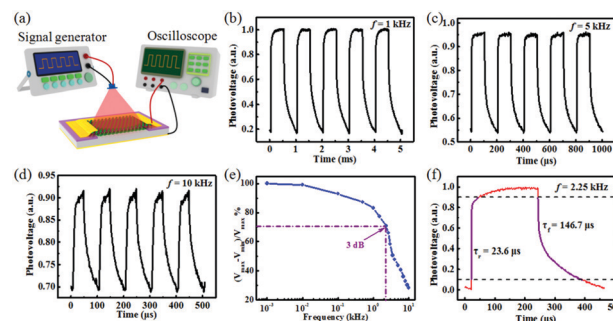


**Fig. 5** (a) Schematic of the setup for measuring the response speed. Photoresponse of the  $\gamma\text{-In}_2\text{Se}_3/\text{GaAs}$  heterojunction photodetector under a 660 nm pulsed laser signal with different frequencies: (b) 1 kHz, (c) 5 kHz and (d) 10 kHz, respectively. (e) Relative balance  $(V_{\text{max}} - V_{\text{min}})/V_{\text{max}}$  *versus* frequency of incident light, showing 3 dB cutoff frequency of about 2.25 kHz. (f) Single magnified photoresponse at 2.25 kHz for estimating the response and the recovery time.

respectively, are plotted in Fig. 5b–d. Obviously, the detector could show an outstanding photo-switching performance with decent repeatability under all the light conditions. The frequency-dependent relative balance  $(V_{\text{max}} - V_{\text{min}})/V_{\text{max}}$  of the photoresponse is further depicted in Fig. 5e, which shows slow decay of the relative balance with the increased switching frequency. Specifically, the value was still larger than 28% even when the frequency was as high as 10 kHz. What is more, it was observed that the 3 dB frequency (the frequency at which the photoresponse declines to 70.7% of its highest value) was located at about 2.25 kHz, suggesting that the present photodetector can work well under light illumination conditions with a wide range of switching frequencies. In addition, the rise time  $\tau_r$  (the duration required for the response to increase from 10% to 90% of its maximum value) and the fall time  $\tau_f$  (the duration required for the response to decline from 90% to 10% of its maximum value)<sup>44</sup> can be estimated to be 23.6 and 146.7  $\mu\text{s}$ , respectively, by analyzing the single magnified photoresponse curve at a frequency of 2.25 kHz (as shown in Fig. 5f). It is noted that the response speed is much faster than the time resolution of human eyes (42 ms), which is of pivotal importance for many applications, such as target detection and safety monitoring.

To evaluate the feasibility of the  $\gamma\text{-In}_2\text{Se}_3/\text{GaAs}$  heterojunction photodetector array for integrated device purposes, the uniformity and reliability of the photoresponse properties of all the 10 device units were first explored. For the convenience of electrical characterization, the devices were fixed onto a printed circuit board (PCB), as shown in the optical photograph

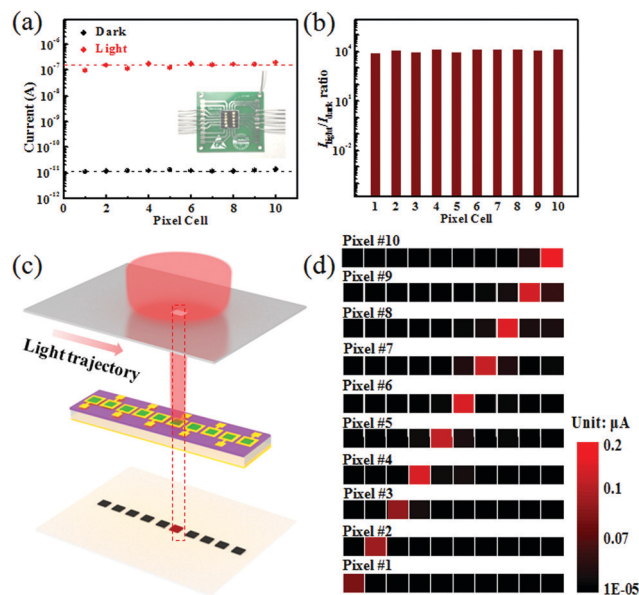


**Fig. 6** (a) Photocurrent and dark current for each of the pixel devices of the  $1 \times 10$   $\gamma\text{-In}_2\text{Se}_3/\text{GaAs}$  heterojunction photodetector array. The inset shows the optical photograph of a typical photodetector array which was fixed onto a printed circuit board (PCB). (b)  $I_{\text{light}}/I_{\text{dark}}$  ratio for each pixel device. (c) Schematic illustration for the real-time light trajectory tracking. (d) Change of the photocurrent when the light spot went through the corresponding pixel.

(the inset of Fig. 6a). The  $I$ - $V$  curves in the dark and upon 660 nm light illumination (light intensity:  $0.85 \text{ mW cm}^{-2}$ ) of each unit device were recorded separately and are plotted in Fig. S5 (ESI<sup>†</sup>). It was found that all the devices showed consistent  $I$ - $V$  characteristics both in the dark and upon light illumination. Furthermore, the values of the dark current and the photocurrent and the  $I_{\text{light}}/I_{\text{dark}}$  ratio of all the devices were extracted and are displayed in Fig. 6a and b. The dark currents were in the range of  $1.11 \times 10^{-11}$  to  $1.35 \times 10^{-11}$  A with an average value of  $1.13 \times 10^{-11}$  A, and the photocurrents were in the range of  $9.67 \times 10^{-8}$  to  $1.90 \times 10^{-7}$  A with an average value of  $1.50 \times 10^{-7}$  A at zero bias (Fig. 6a). Also, the devices had the majority of the  $I_{\text{light}}/I_{\text{dark}}$  ratio of about  $1.4 \times 10^4$ , in spite of the minor unit-to-unit variation in both the photocurrent and dark current (as shown in Fig. 6b). The above findings suggested the good uniformity of our heterojunction photodetector array, which enables potential use for integrated device applications.

The fast response of the  $\gamma\text{-In}_2\text{Se}_3/\text{GaAs}$  heterojunction photodetector endows our photodetector array with the ability to monitor fast-moving objects, which is a critical application for optical sensing. Fig. 6c schematically illustrates a setup for tracking the trajectory of a moving visible light spot. The light spot was obtained by placing a lab-built shadow mask with a small hollow hole in front of the 660 nm LED light source. When moving the shadow mask along a straight line, the light spot would project successively on the device unit from unit no. 1 to unit no. 10. Then the currents of all the 10 device units were recorded and summarized in the form of 2D contrast maps with different colors denoting varied current levels (as shown in Fig. 6d). Obviously, with the light spot moving

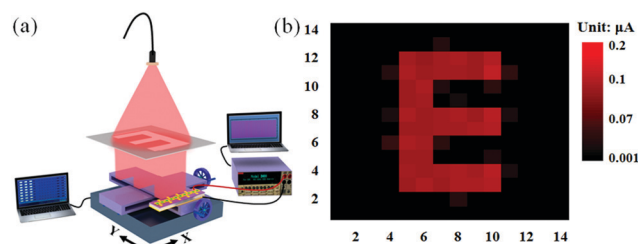


**Fig. 7** (a) Schematic illustration of the visible light imaging system. (b) Corresponding 2D current mapping of the linear photodetector arrays upon 660 nm illumination.

through no. unit 1 to no. unit 10, the current of the corresponding device unit increased remarkably, while those of the other device units remained unchanged. The result reveals that the present photodetector array can properly record the motion trajectory of a light spot, and also suggests great potential for light trajectory tracking. Note that the spatial resolution of the trajectory tracking can be further improved by miniaturization of the devices and/or by increasing the number of the device units, and real-time trajectory tracking of high-speed targets is also realizable *via* real-time data capture and analysis of our photodetector array.<sup>45</sup>

Finally, the preliminary function of the heterojunction photodetector array to work as a visible image sensor is demonstrated. As schematically displayed in Fig. 7a, a lab-made shadow mask with a hollow "E" pattern ( $10 \text{ mm} \times 10 \text{ mm}$ ) was laid between the 660 nm light irradiation and the photodetector array was fixed on a platform of a stepper motor. The stepper motor then drove the photodetector array to move progressively along the  $Y$  axis at a step length of 1 mm, during which the electrical signals of all the 10 device units were recorded separately. The results were incorporated into a  $10 \times 10$  2D current contrast map. Remarkably, as shown in Fig. 7b, the shape of the "E" pattern could be clearly identified with a suitable spatial resolution, implying a good possibility in the field of visible light image sensing.

## Conclusions

In summary, we have presented the scalable fabrication of a  $\gamma\text{-In}_2\text{Se}_3/\text{GaAs}$  heterostructure-based photodetector array with  $1 \times 10$  device units through a combined photolithography and radio-frequency magnetron sputtering deposition method. Such heterojunctions could exhibit an apparent photovoltaic behavior, and could therefore operate as self-driven photodetectors with a good uniformity in the device performance. Upon 660 nm light illumination, the  $I_{\text{light}}/I_{\text{dark}}$  ratio, responsivity ( $R$ ), specific detectivity ( $D^*$ ) and response speed of the representative device reached  $1.29 \times 10^4$ ,  $0.25 \text{ A W}^{-1}$ ,  $7.34 \times 10^{12}$  Jones and  $23.6/146.7 \text{ } \mu\text{s}$  (rise/fall times), respectively, at zero bias. Moreover, the present photodetector array showed preliminary functions of monitoring a fast-moving photon signal and recording an "E" image produced by visible light illumination, implying a possibility for practical optoelectronic applications including real-time light trajectory tracking and visible light image sensing.

## Conflicts of interest

There are no conflicts to declare.

## Acknowledgements

This work was supported by the National Natural Science Foundation of China (NSFC, No. 62074048, 61675062 and 51902078), the Anhui Provincial Natural Science Foundation (2008085MF205) and the Fundamental Research Funds for the Central Universities (PA2020GDKC0014, JZ2020HGTB0051, JZ2018HGXC0001, and JZ2018HGPPB0275).

## Notes and references

- H. Chen, H. Liu, Z. Zhang, K. Hu and X. Fang, *Adv. Mater.*, 2016, **28**, 403–433.
- F. Teng, K. Hu, W. Ouyang and X. Fang, *Adv. Mater.*, 2018, **30**, 1706262.
- W. Wu, X. Wang, X. Han, Z. Yang, G. Gao, Y. Zhang, J. Hu, Y. Tan, A. Pan and C. Pan, *Adv. Mater.*, 2019, **31**, 1805913.
- T. Mueller, F. Xia and P. Avouris, *Nat. Photonics*, 2010, **4**, 297–301.
- E. Wu, D. Wu, C. Jia, Y. Wang, H. Yuan, L. Zeng, T. Xu, Z. Shi, Y. Tian and X. Li, *ACS Photonics*, 2019, **6**, 565–572.
- C. Xie and F. Yan, *Small*, 2017, **13**, 1701822.
- F. Liao, J. Deng, X. Chen, Y. Wang, X. Zhang, J. Liu, H. Zhu, L. Chen, Q. Sun, W. Hu, J. Wang, J. Zhou, P. Zhou, D. W. Zhang, J. Wan and W. Bao, *Small*, 2019, **16**, 1904369.
- N. Guo, L. Xiao, F. Gong, M. Luo, F. Wang, Y. Jia, H. Chang, J. Liu, Q. Li, Y. Wu, C. Shan, Y. Xu, P. Zhou and W. Hu, *Adv. Sci.*, 2020, **7**, 1901637.
- M. Long, Y. Wang, P. Wang, X. Zhou, H. Xia, C. Luo, S. Huang, G. Zhang, H. Yan, Z. Fan, X. Wu, X. Chen, W. Lu and W. Hu, *ACS Nano*, 2019, **13**, 2511–2519.
- L.-H. Zeng, S.-H. Lin, Z.-J. Li, Z.-X. Zhang, T.-F. Zhang, C. Xie, C.-H. Mak, Y. Chai, S. P. Lau, L.-B. Luo and Y. H. Tsang, *Adv. Funct. Mater.*, 2018, **28**, 1705970.
- L.-B. Luo, D. Wang, C. Xie, J.-G. Hu, X.-Y. Zhao and F.-X. Liang, *Adv. Funct. Mater.*, 2019, **29**, 1900849.
- Z. He, J. Guo, S. Li, Z. Lei, L. Lin, Y. Ke, W. Jie, T. Gong, Y. Lin, T. Cheng, W. Huang and X. Zhang, *Adv. Mater. Interfaces*, 2020, **24**, 1901848.
- H.-W. Yang, H.-F. Hsieh, R.-S. Chen, C.-H. Ho, K.-Y. Lee and L.-C. Chao, *ACS Appl. Mater. Interfaces*, 2018, **10**, 5740–5749.
- W. Ding, J. Zhu, Z. Wang, Y. Gao, D. Xiao, Y. Gu, Z. Zhang and W. Zhu, *Nat. Commun.*, 2017, **8**, 14956.
- X. Zhou, L. Gan, W. Tian, Q. Zhang, S. Jin, H. Li, Y. Bando, D. Golberg and T. Zhai, *Adv. Mater.*, 2015, **27**, 8035–8041.
- J. Yao, Z. Zheng and G. Yang, *Adv. Funct. Mater.*, 2017, **27**, 1701823.
- J. Wang, H. Fang, X. Wang, X. Chen, W. Lu and W. Hu, *Small*, 2017, **13**, 1700894.
- M. Long, P. Wang, H. Fang and W. Hu, *Adv. Funct. Mater.*, 2019, **29**, 1803807.
- M. Lin, D. Wu, Y. Zhou, W. Huang, W. Jiang, W. Zheng, S. Zhao, C. Jin, Y. Guo, H. Peng and Z. Liu, *J. Am. Chem. Soc.*, 2013, **135**, 13274–13277.
- J. Zhou, Q. Zeng, D. Lv, L. Sun, L. Niu, W. Fu, F. Liu, Z. Shen, C. Jin and Z. Liu, *Nano Lett.*, 2015, **15**, 6400–6405.
- W. Feng, F. Gao, Y. Hu, M. Dai, H. Li, L. Wang and P. Hu, *Nanotechnology*, 2018, **29**, 445205.
- J. Yao, Z. Deng, Z. Zheng and G. Yang, *ACS Appl. Mater. Interfaces*, 2016, **8**, 20872–20879.
- Z. Zheng, J. Yao, J. Xiao and G. Yang, *ACS Appl. Mater. Interfaces*, 2016, **8**, 20200–20211.
- R. B. Jacobs-Gedrim, M. Shanmugam, N. Jain, C. A. Durcan, M. T. Murphy, T. M. Murray, R. J. Matyi, R. L. Moore and B. Yu, *ACS Nano*, 2014, **8**, 514–521.
- B. Tang, L. Hou, M. Sun, F. Lv, J. Liao, W. Ji and Q. Chen, *Nanoscale*, 2019, **11**, 12817–12828.
- J. O. Island, S. I. Blanter, M. Buscema, H. S. J. van der Zant and A. Castellanos-Gomez, *Nano Lett.*, 2015, **15**, 7853–7858.
- S. Chen, X. Liu, X. Qiao, X. Wan, K. Shehzad, X. Zhang, Y. Xu and X. Fan, *Small*, 2017, **13**, 1604033.
- Z. Zheng, J. Yao, B. Wang, Y. Yang, G. Yang and J. Li, *ACS Appl. Mater. Interfaces*, 2017, **9**, 43830–43837.
- C.-Y. Wu, J.-W. Kang, B. Wang, H.-N. Zhu, Z.-J. Li, S.-R. Chen, L. Wang, W.-H. Yang, C. Xie and L.-B. Luo, *J. Mater. Chem. C*, 2019, **7**, 11532–11539.
- J. Jiang, N. Li, J. Zou, X. Zhou, G. Eda, Q. Zhang, H. Zhang, L.-J. Li, T. Zhai and A. T. A. Wee, *Chem. Soc. Rev.*, 2019, **48**, 4639–4654.
- J. D. Yao, Z. Q. Zheng and G. W. Yang, *Prog. Mater. Sci.*, 2019, **106**, 100573.
- W. Zheng, T. Xie, Y. Zhou, Y. L. Chen, W. Jiang, S. Zhao, J. Wu, Y. Jing, Y. Wu, G. Chen, Y. Guo, J. Yin, S. Huang, H. Q. Xu, Z. Liu and H. Peng, *Nat. Commun.*, 2015, **6**, 6972.
- Z. Q. Zheng, J. D. Yao and G. W. Yang, *J. Mater. Chem. C*, 2016, **4**, 8094–8103.
- X. F. Wei, L. W. Lia, H. G. Feng, J. B. Gong, K. Jiang and S. L. Xue, *Ceram. Int.*, 2020, **46**, 1026–1032.
- C.-H. Ho, C.-H. Lin, Y.-P. Wang, Y.-C. Chen, S.-H. Chen and Y.-S. Huang, *ACS Appl. Mater. Interfaces*, 2013, **5**, 2269–2277.
- M. Buscema, J. O. Island, D. J. Groenendijk, S. I. Blanter, G. A. Steele, H. S. J. van der Zant and A. Castellanos-Gomez, *Chem. Soc. Rev.*, 2015, **44**, 3691–3718.
- X. Li, M. Zhu, M. Du, Z. Lv, L. Zhang, Y. Li, Y. Yang, T. Yang, X. Li, K. Wang, H. Zhu and Y. Fang, *Small*, 2016, **12**, 595–601.
- L. Wang, J. Jie, Z. Shao, Q. Zhang, X. Zhang, Y. Wang, Z. Sun and S. T. Lee, *Adv. Funct. Mater.*, 2015, **25**, 2910–2919.
- C. Xie, P. You, Z. Liu, L. Li and F. Yan, *Light: Sci. Appl.*, 2017, **8**, e17023.
- L. B. Luo, J. J. Chen, M. Z. Wang, H. Hu, C. Y. Wu, Q. Li, L. Wang, J. A. Huang and F. X. Liang, *Adv. Funct. Mater.*, 2014, **24**, 2794–2800.
- Z. Xu, S. Lin, X. Li, S. Zhang, Z. Wu, W. Xu, Y. Lu and S. Xu, *Nano Energy*, 2016, **23**, 89–96.



- 42 B. D. Boruah, A. Mukherjee and A. Misra, *Nanotechnology*, 2016, **27**, 095205.
- 43 L. H. Zeng, D. Wu, S. H. Lin, C. Xie, H. Y. Yuan, W. Lu, S. P. Lau, Y. Chai, L. B. Luo, Z. J. Li and Y. H. Tsang, *Adv. Funct. Mater.*, 2019, **29**, 1806878.
- 44 Y.-Y. Wang, Y.-D. Wu, W. Peng, Y.-H. Song, B. Wang, C.-Y. Wu and Y. Lu, *Nanoscale*, 2018, **10**, 18502–18509.
- 45 K. Liu, W. Wang, Y. Yu, X. Hou, Y. Liu, W. Chen, X. Wang, J. Lu and Z. Ni, *Nano Lett.*, 2019, **19**, 8132–8137.